

Anomalous strain-dependent thermal conductivity in the metal-organic framework HKUST-1

Hongzhao Fan,^{1,2} Penghua Ying³, Zheyong Fan,⁴ Yue Chen⁵, Zhigang Li,¹ and Yanguang Zhou^{1,2,*}

¹Department of Mechanical and Aerospace Engineering, The Hong Kong University of Science and Technology, Clear Water Bay, Kowloon, Hong Kong SAR

²HKUST Shenzhen-Hong Kong Collaborative Innovation Research Institute, Futian, Shenzhen, Guangdong, China

³School of Science, Harbin Institute of Technology, Shenzhen 518055, China

⁴College of Physical Science and Technology, Bohai University, Jinzhou 121013, China

⁵Department of Mechanical Engineering, The University of Hong Kong, Pokfulam Road, Hong Kong SAR



(Received 1 July 2023; revised 17 October 2023; accepted 2 January 2024; published 19 January 2024)

Metal-organic frameworks (MOFs) have often been used for gas storage owing to their high surface areas and nanoscale pores, where they are packed in the tank. The concomitant exothermicity and endothermicity during the gas storage process strongly affect their storage capacity. Understanding the thermal transport in MOFs under mechanical strain is critical to maximizing the gas uptake capacity of MOFs. Here, we systematically investigate the thermal transport in a typical MOF (i.e., HKUST-1 or equivalently MOF-199) considering the external mechanical strain using molecular dynamics simulations. We find that the thermal conductivity of HKUST-1 decreases with compressive strain and increases with tensile strain, which is contradictory to the classical Liebfried and Schrömann theory, i.e., the thermal conductivity of crystals should increase with applied compression. Our spectral analysis further shows that the abnormal strain-dependent thermal conductivity can be well explained by the phonon-gas theory. We find that the relaxation time of vibrations in HKUST-1 decreases when compressive strain is applied. This is because the anharmonicity of compressed HKUST-1 increases compared with that of pristine HKUST-1. The anharmonicity of HKUST-1 decreases when tensile strain is applied, and thus, the corresponding vibrational relaxation time increases. Meanwhile, the vibrational group velocity decreases or increases for compressed or tensile HKUST-1, respectively. This is due to the compression- or stretch-induced shift of vibrational branches caused by the structural softening and hardening. Therefore, the thermal conductivity of HKUST-1 decreases with compressive strain even though the volumetric heat capacity of compressed HKUST-1 increases. The thermal conductivity of HKUST-1 increases with tensile strain, though the corresponding volumetric heat capacity decreases. Here, we provide a fundamental understanding of the thermal transport mechanisms in MOFs considering mechanical strain, which offers guidance for the thermal management design in these corresponding gas storage applications.

DOI: [10.1103/PhysRevB.109.045424](https://doi.org/10.1103/PhysRevB.109.045424)

I. INTRODUCTION

Metal-organic frameworks (MOFs) have been regarded as promising candidates for gas storage owing to their high internal surface areas and nanoscale pores. However, the concomitant exothermicity and endothermicity during gas adsorption and desorption processes strongly affects the performance of MOFs, e.g., the reduction of adsorption capacity [1] and sharp temperature spikes [2]. During the gas adsorption process, there is a decrease in the residual attractive forces present on the surface of the adsorbent (i.e., MOF here), leading to a reduction in the surface energy of the adsorbent, which evolves as heat. Therefore, the enthalpy of gas adsorption is negative, and the gas adsorption is essentially an exothermic process. In contrast, gas desorption is an endothermic process. The concomitant exothermicity and endothermicity during the gas storage process can cause significant temperature rises and drops in the gas storage systems, which in turn affects the

corresponding usable gas capacity. For instance, the natural gas storage cylinders could be cooled by as much as 37 °C at a discharge rate for a typical driving speed, which resulted in a 25% reduction in CH₄ storage capacity compared with isothermal desorption [3]. Moreover, in realistic gas storage systems, MOFs are usually packed in a tank [4,5] and therefore are deformed. Therefore, the influence of mechanical deformation on the thermal conductivity of MOFs must be known to determine and manage the operating temperatures of the corresponding devices, which is critical for the gas uptake capacity of MOFs.

There have been previous efforts to quantify the influence of mechanical strain on thermal conductivity κ in MOFs. Han *et al.* [6] investigated the strain effect on the thermal conductivity of MOF-5 by molecular dynamics (MD) simulations. They found that the thermal conductivity of MOF-5 decreased with tensile strain and increased with compressive strain. Further first-principles calculations also showed that the thermal conductivity of MOF-5 decreased with external tensile strain [7]. Ying *et al.* [8] studied the pressure effect on the thermal conductivity of pristine and halogen-substituted

*maeyzhou@ust.hk

MOF zeolitic imidazolate framework (ZIF)-8. They found that the applied pressure would lead to a dense phase of ZIF-8 and a higher thermal conductivity than that of the porous phase at lower pressures. All these results show that the compression P will increase the thermal conductivity of MOFs, which agrees well with the classical Liebfried and Schlömann (LS) theory [9,10], i.e., $\frac{dk}{dP} > 0$. It is therefore easy to hypothesize that the thermal conductivity of crystalline MOFs increases (decreases) under compression (tension). Moreover, both experiments [11] and simulations [12–14] showed that the heat carriers in MOFs might behave as nonpropagating quasiparticles, which may lead to the corresponding thermal conductivity deviating from the predictions of the classic theory, i.e., the pressure-dependent thermal conductivity of MOFs does not follow the LS theory.

In this paper, we report on an anomalous strain-dependent thermal conductivity in a typical MOF crystal (i.e., HKUST-1 or equivalently MOF-199) using atomistic simulations, which is against the prediction of the LS theory. Three force fields (FFs) that are derived based on various methods are applied to depict the interatomic interactions in HKUST-1 and validate our numerical results. Our results show that the thermal conductivity of HKUST-1 is monotonically improved by tensile strain and depressed by compressive strain in the crystal phase. The thermal conductivity of HKUST-1 is found to increase by ~ 2 times, i.e., from ~ 0.7 to ~ 1.4 W/mK, by applying external mechanical strain. Our spectral vibrational analysis further shows that the reduction (enhancement) of thermal conductivity in HKUST-1 caused by the compression (tensile strain) results from the change of vibrational anharmonicity and group velocity, which stems from the shrinkage of the atomic interspace and the structural softening-hardening.

II. SIMULATION AND CALCULATION DETAILS

A. Interatomic FF

In this paper, we performed MD simulations to evaluate the strain dependence of thermal conductivity in HKUST-1. Meanwhile, for comparison, we have applied three interatomic FFs [2,15,16] to depict the interactions of atoms in HKUST-1. The first adopted FF was developed by Zhao *et al.* [15], in which parameters were fitted based on the first-principles calculations and existing potentials [17–19]. This FF has been demonstrated to describe the crystal structure, negative thermal expansion, vibrational properties, and adsorption behavior of HKUST-1 [15] well and has been widely used to model the thermal transport in HKUST-1 [20–23]. The second FF we used was developed by Wieme *et al.* [2], which was derived by fitting the potential energy surface obtained from first-principles calculations. The thermal properties, including heat capacity and the thermal expansion coefficient calculated using this FF, agree well with experimental measurements [2]. The last FF used to depict HKUST-1 was developed under the framework of the third generation of neuroevolution potential (NEP3) [24]. The MD simulations with Zhao's and Wieme's FFs are performed by LAMMPS [25]. The MD simulations with NEP3 FF are carried out by GPUMD [16]. For Zhao's and Wieme's FFs, the interatomic interactions

are described by the terms of covalent (bond, angle, dihedral, and out-of-plane), electrostatic, and van der Waals interactions [2,15]. The long-range electrostatic interactions in our simulations are solved by the particle-particle particle-mesh solver with a relative force error of 10^{-5} [26]. For NEP3 FF, the total energy of the system is taken as a sum of the site energies. The site energy of atom i is a neural network model that takes a descriptor vector \mathbf{q}^i as the input:

$$U_i = \sum_{\mu=1}^{N_{\text{neu}}} \omega_{\mu}^{(1)} \tanh \left[\sum_{v=1}^{N_{\text{des}}} \omega_{\mu v}^{(0)} q_v^i - b_{\mu}^{(0)} \right] - b^{(1)}, \quad (1)$$

where N_{neu} is the number of neurons within a single hidden layer, N_{des} is the number of components of the descriptor vector, $\tanh(x)$ is the activation function, $\omega^{(0)}$ and $\omega^{(1)}$ are trainable weights, and $b^{(0)}$ and $b^{(1)}$ are bias parameters in the neural network. The atomic environment descriptor is decomposed into radial and angular parts. The radial descriptor is constructed by linear combinations of Chebyshev basis functions, and the angular descriptor is built using the atomic cluster expansion approach [16]. The dataset for training NEP3 FF was constructed using energy, atomic force, and virial data of reference structures computed by static density functional theory (DFT) calculations. The reference structures are first obtained by selecting structures from *ab initio* MD (AIMD). The primitive cell of HKUST-1 containing 156 atoms is used in the AIMD simulations. The AIMD simulations were conducted in the NVT (constant number of particles, volume, and temperature) ensemble controlled by a Nosé-Hoover thermostat [27] with an energy threshold of 10^{-5} eV and an energy cutoff of 520 eV for the electronic self-consistent calculation. The Γ -point K mesh was sampled in the Brillouin zone. A time step of 1 fs was used. The temperatures ranging from 10 to 800 K are considered in the AIMD calculation. Here, 560 different structures were selected from all 10 000 structures in our AIMD simulations to construct the dataset. Then 100 perturbed structures generated by the DPDATA package [28] were added to the dataset of reference structures, in which the deformations of the structures are in the range of -3 to 3% , and atomic displacements were set with a standard deviation of 0.1 Å. Static DFT calculations of these 660 structures with a threshold of 10^{-7} eV and an energy cutoff of 600 eV were then implemented to obtain accurate energy, atomic force, and virial data. The static DFT calculations were based on the Perdew-Burke-Ernzerhof functional [29] and the projector augmented-wave method [30] and were implemented by VASP [31,32]. The K mesh adopted in our static DFT calculations was generated using the Monkhorst-Pack (MP) approach with a density of $0.2/\text{\AA}$ and a Gaussian smearing width of 0.05 eV. Using the static DFT calculated atomic data of these 660 structures, the first NEP model is trained. Then using the first NEP model, the NEP-driven MD simulations were performed, and 100 structures were selected from MD simulations. Combining with the previous 660 structure, the second NEP model was trained based on the static DFT calculated data of the 760 structures. After the second round of NEP-driven MD simulations, we finally obtained a total of 860 reference structures. The final NEP model was trained based on the static DFT

calculated data of these 860 reference structures. Details for the DFT calculations and NEP3 FF can be found in Ref. [33].

B. MD simulations

The thermal conductivity of HKUST-1 was calculated using nonequilibrium MD (NEMD) and homogeneous NEMD (HNEMD) simulations. The NEMD simulations were performed using the LAMMPS package, and the HNEMD simulations were implemented by the GPUMD package. In all MD simulations, the timestep is 0.5 fs, and periodic boundary conditions are applied along three directions. For the NEMD simulations, systems with a size of $2 \times 2 \times 60$ unit cells (UCs) were first relaxed in an NPT (constant number of particles, pressure, and temperature) ensemble for 500 ps with various strains. The corresponding length of the systems in our NEMD simulations is 149.9 nm, which is long enough to involve most of the long-wavelength phonons [23]. Two regions with a thickness of 1.36 nm at the ends of the model were fixed in our NEMD simulations. Two layers of atoms closing to the fixed regions with a thickness of 1.36 nm were coupled with Langevin thermostats and selected as the heat source and sink, respectively. The temperature gradient in the systems is ~ 0.133 K/Å. We checked the effect of the temperature gradient on the calculated thermal conductivity and found this temperature gradient can give reliable results. Each NEMD simulation runs 7 ns, and the last 3 ns were used to calculate thermal conductivity based on Fourier's laws:

$$\kappa = \frac{Q}{A \cdot \nabla T}, \quad (2)$$

where Q is the heat current extracted from the Langevin thermostats, A is the cross-section area, and ∇T is the temperature gradient in the system.

In all our HNEMD simulations, the thermal conductivity is calculated by [34]

$$\kappa = \frac{1}{t} \int_0^t \frac{J(\tau)}{TVF_e} d\tau, \quad (3)$$

in which T is the temperature of the system, V is the volume of the system, and J is the heat current induced by the driving force \vec{F}_i^{ext} of the atom i . The driving force on atoms \vec{F}_i^{ext} is related to the parameter F_e , which is set to $1.5 \mu\text{m}^{-1}$ in all HNEMD simulations. The thermal conductivity calculated by HNEMD simulations is averaged by five independent simulations. Strain was applied by deforming the structure of HKUST-1 along three directions directly in our HNEMD simulations.

C. Vibrational mean free path spectrum

To quantitatively characterize the thermal transport in HKUST-1, we calculated the corresponding vibrational mean free path (MFP) spectrum. In NEMD simulation, the heat current across an imaginary interface can be calculated using

$$Q_{\text{left} \rightarrow \text{right}} = \sum_{i \in \text{left}} \sum_{j \in \text{right}} \left(\frac{\partial U_j}{\partial \vec{r}_i} \cdot \vec{v}_i - \frac{\partial U_i}{\partial \vec{r}_j} \cdot \vec{v}_j \right), \quad (4)$$

in which U is the potential energy, \vec{v} is atomic velocity, \vec{r} is atomic position, and left and right denote the left and right

sides of the imaginary interface, respectively. The spectral heat current in NEMD simulations can be written in the form of [35–38]

$$Q(\omega) = 2 \sum_{i \in \text{left}} \sum_{j \in \text{right}} \text{Re} \left\{ \int_0^{+\infty} \left[\frac{\partial U_j}{\partial \vec{r}_i} \Big|_\tau \vec{v}_i(0) - \frac{\partial U_i}{\partial \vec{r}_j} \Big|_\tau \vec{v}_j(0) \right] e^{-i\omega\tau} d\tau \right\}. \quad (5)$$

The spectral thermal conductivity then can be calculated as

$$\kappa(\omega) = \frac{Q(\omega)}{A \cdot \nabla T}. \quad (6)$$

Based on the Landauer theory [39–41], the spectral heat current across a junction between two leads with different equilibrium heat-bath temperatures (i.e., T_L and T_R) is expressed as

$$Q(\omega) = \hbar\omega[f_L(\omega) - f_R(\omega)]\Gamma(\omega), \quad (7)$$

where f is the phonon distribution function at the heat-bath temperature, which is equal to the classical limit of the Boltzmann distribution in MD simulations. Here, $\Gamma(\omega)$ is the phonon transmission function. Thus, the spectral thermal conductance $G(\omega)$ can be calculated via

$$G(\omega) = \frac{\hbar\omega[f_L(\omega) - f_R(\omega)] \cdot \Gamma(\omega)}{A(T_L - T_R)} = \frac{\hbar\omega\Delta f(\omega) \cdot \Gamma(\omega)}{A\Delta T} \approx \frac{\hbar\omega\partial f(\omega)}{\partial T} \frac{\Gamma(\omega)}{A} \stackrel{\text{classic limit}}{=} k_b \frac{\Gamma(\omega)}{A}, \quad (8)$$

in which ΔT is the temperature difference between two thermal baths in the simulation system. Therefore, the phonon transmission function in NEMD simulations can be approximately calculated via

$$\Gamma(\omega) = \frac{Q(\omega)}{k_b\Delta T}. \quad (9)$$

Meanwhile, the phonon transmission function can also be written as [38,40,42]

$$\Gamma(\omega) = \frac{\Gamma_b(\omega)}{1 + L/\Lambda(\omega)}, \quad (10)$$

where $\Lambda(\omega)$ is the vibrational MFP spectrum, L is the length of the system, and $\Gamma_b(\omega)$ is the ballistic phonon transmission function. Hence, by substituting Eq. (9) into Eq. (10), the phenomenological MFP in NEMD simulations can be calculated by

$$\Lambda(\omega) = \frac{Q(\omega) \cdot L/\Delta T}{Q_b(\omega)/\Delta T_b - Q(\omega)/\Delta T}, \quad (11)$$

in which $Q_b(\omega)$ and ΔT_b are spectral heat current and temperature difference of two thermal baths under ballistic thermal transport, respectively. To mimic the ballistic thermal transport in NEMD simulations, the system length is set as one lattice constant, and the temperature difference between two thermal baths is set as 60 K.

D. Spectral energy density of vibrations

We also calculated the vibrational band structures of HKUST-1 under various strains using spectral energy density

(SED). At a specific \vec{k} , the vibrational SED can be calculated by [43]

$$\Phi(\vec{k}) = \frac{1}{4\pi\tau_0 N} \sum_{\alpha} \sum_b^B m_b \left| \int_0^{\tau_0} \sum_{n_{x,y,z}}^N v_{\alpha} \left(\frac{n_{x,y,z}}{b}; t \right) \times \exp \left[i \vec{k} \cdot \vec{r} \left(\frac{n_{x,y,z}}{b}; 0 \right) - i\omega t \right] dt \right|^2, \quad (12)$$

where N is the number of unit cells in the supercell, α denotes the direction, m_b is the atomic mass of the atom b , τ_0 is total simulation time, $n_{x,y,z}$ is the index number of the unit cell along the x , y , and z direction, $v_{\alpha} \left(\frac{n_{x,y,z}}{b}; t \right)$ is the velocity of atom b in the unit cell $n_{x,y,z}$ along the α direction, and $\vec{r} \left(\frac{n_{x,y,z}}{b}; 0 \right)$ is the equilibrium position of the unit cell $n_{x,y,z}$. In all our SED calculations in which the interatomic interactions are depicted using Zhao's FF, a model with a size of $2 \times 2 \times 60$ UCs is used. While the systems are depicted using NEP3 FF, the size of the systems is $1 \times 1 \times 60$ UCs in our SED calculations due to the high computational cost. To examine the effect of the applied strain, the models are firstly relaxed under the NPT ensemble for 0.5 ns and then switched to the NVE ensemble for another 1 ns to collect the data. Then the SED spectrum is calculated using the collected data and averaged twice. The strength of phonon scattering can be reflected by the phonon lifetime, which is calculated by fitting the SED curve. The half-line width $\gamma(\vec{k})$ at the center point of $\omega_0(\vec{k})$ can be obtained from Lorentzian function fitting [43,44]:

$$\Phi(\vec{k}) = C_0(\vec{k}) \frac{\gamma(\vec{k})/\pi}{[\omega_0(\vec{k}) - \omega]^2 + \gamma^2(\vec{k})}, \quad (13)$$

where $C_0(\vec{k})$ is a mode-dependent constant. Then the phonon lifetime $\tau(\vec{k})$ is given by

$$\tau(\vec{k}) = \frac{1}{2\gamma(\vec{k})}. \quad (14)$$

III. RESULTS AND DISCUSSIONS

A. Anomalous strain-dependent thermal conductivity

As discussed above, for HKUST-1 depicted using different FFs, the mechanical strain is applied in our simulations via different approaches. When we calculated the thermal conductivity in the framework of NEMD simulations, the systems relax in the NPT ensemble under different pressures, in which the pressures are applied along all three directions simultaneously. When we calculated the thermal conductivity using HNEMD simulations, the strain was applied to the systems by directly rescaling the atomic coordinates along all three directions. The systems were then relaxed in the NVT ensemble for 100 ps. Therefore, the applied strain range in simulations depicted using different FFs is slightly different. The applied strain in our simulations ranges from ~ -1 to $\sim 2\%$, where negative strain means that the lattice is compressed, and positive strain indicates that the lattice is stretched. It is noted that HKUST-1 is still a crystal and has no phase transition under applied strain. Authors of previous experimental studies [45–47] have demonstrated that

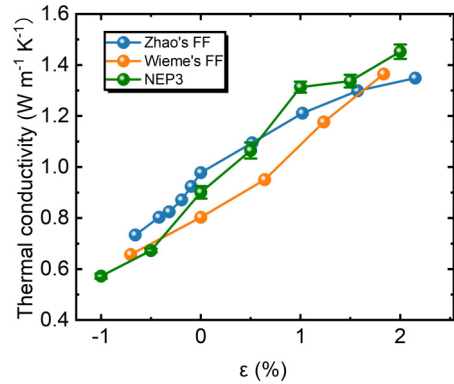


FIG. 1. The calculated thermal conductivities of HKUST-1 at 300 K under different strains. The blue, orange, and green circle points represent the thermal conductivities of HKUST-1 calculated based on the force fields (FFs) of Zhao *et al.* [15], Wieme *et al.* [2], and the third generation of neuroevolution potential (NEP3) FF [33], respectively.

HKUST-1 samples can be deformed in a wide range, which covers the applied strain in our simulations. Our MD results (Fig. 1) show that the thermal conductivity of HKUST-1 decreases (increases) with applied compressive strain (tensile strain), which is contradictory to the classical LS theory [9,48] and other simulation results of MOFs [6,8]. The largest compressive strain applied to HKUST-1 depicted by NEP3 FF is -1% , which leads to a thermal conductivity of ~ 0.57 W/mK. For HKUST-1 described using Zhao's and Wieme's FFs, the largest compressive strains that can be applied are -0.66 and -0.70% , respectively. The corresponding calculated thermal conductivities are ~ 0.73 and ~ 0.66 W/mK for HKUST-1 depicted using Zhao's and Wieme's FFs, respectively. When applied compressive strain is over the maximum value (i.e., -1% for NEP3 FF, -0.66% for Zhao's FF, and -0.70% for Wieme's FF), the HKUST-1 structures will collapse. The thermal conductivity of HKUST-1 depicted by all three FFs increases monotonically with applied strain to ~ 1.4 W/mK (i.e., at the applied strain of $\sim 2\%$). We emphasize that the thermal conductivities calculated using all three FFs show the same trend and similar values, which demonstrates that the abnormal strain-dependent thermal conductivity of HKUST-1 is self-consistent and does not result from the chosen FF. Thereafter, we select the HKUST-1 depicted using Zhao's FF for our further analysis.

Meanwhile, thermal conductivity contributed by phonons (i.e., the quanta of lattice vibrations) can also be calculated based on the phonon-gas model, i.e., $\kappa \sim c_V v_g^2 \tau$, where c_V , v_g , and τ are the volumetric heat capacity, group velocity, and relaxation time of phonons, respectively. In MD simulations, as all the vibrations are fully occupied, the volumetric heat capacity is then calculated using $c_V = (\langle E^2 \rangle - \langle E \rangle^2)/k_b T^2 V$, in which V is the volume of the system, E is the energy of the system, and $\langle \rangle$ denotes the ensemble average. Therefore, compressive strain and tensile strain should increase and decrease the volumetric heat capacity, respectively. Our calculated results show that the volumetric heat capacity can be increased by 2.93% or decreased by 6.13% compared with

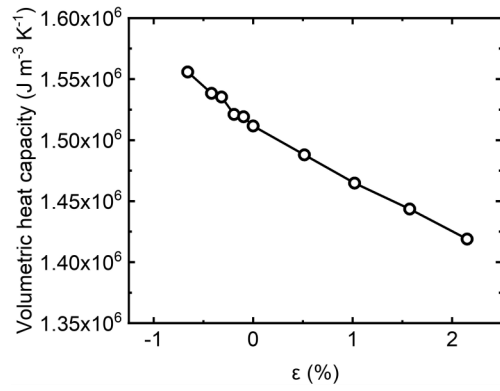


FIG. 2. The volumetric heat capacity of HKUST-1 under different strains.

pristine HKUST-1 by applied compressive strain or tensile strain (Fig. 2), respectively. Authors of several previous studies [8,14,49] showed that the improvement of volumetric heat capacity is the main reason for the enhancement of the thermal conductivity of MOFs. For instance, both Sørensen *et al.* [49] and Zhou *et al.* [14] showed the thermal conductivities of amorphous ZIF-4 and ZIF-62 were higher than that of their crystalline counterparts, which was mainly caused by the higher volumetric heat capacity of the amorphous structures. A similar phenomenon was also observed in ZIF-8 [8,14]. However, comparing the change of c_V (2.93 to -6.13% compared with pristine HKUST-1) with the change of κ (-24.99

to 37.09% compared with pristine HKUST-1), we find that the strain-induced variation of c_V is opposite that of the thermal conductivity. Therefore, the change of phonon properties induced by strain should be responsible for the abnormal strain-dependent thermal conductivity in HKUST-1.

B. Spectral thermal conductivity and MFP

To characterize the thermal transport capability in HKUST-1 under various strains, we calculate the strain-dependent spectral thermal conductivity of HKUST-1 [i.e., Eq. (6) in Sec. II B]. Here, three HKUST-1 structures depicted using Zhao's FF with applied strains of -0.66 , 0 , and 1.02% are chosen as examples to carry out the calculations and analysis. Our calculated results show that the spectral thermal conductivity is generally increased when a tensile strain is applied to HKUST-1 [Fig. 3(a)]. We also calculate the accumulative thermal conductivity of HKUST-1 under three typical strains (i.e., -0.66 , 0 , and 0.12%), as shown in Fig. 3(b). Our results show that the thermal conductivity contributed by the low-frequency vibrations (i.e., <4 THz) apparently decreases when the applied strain changes from compressive to tensile. The contribution of vibrations with frequencies >4 THz to the total thermal conductivity is found to be relatively low when external tensile strain is applied. When the HKUST-1 structure is compressed, the modal thermal conductivities of these low-frequency (i.e., <2 THz) vibrations are largely decreased compared with that without applied strain.

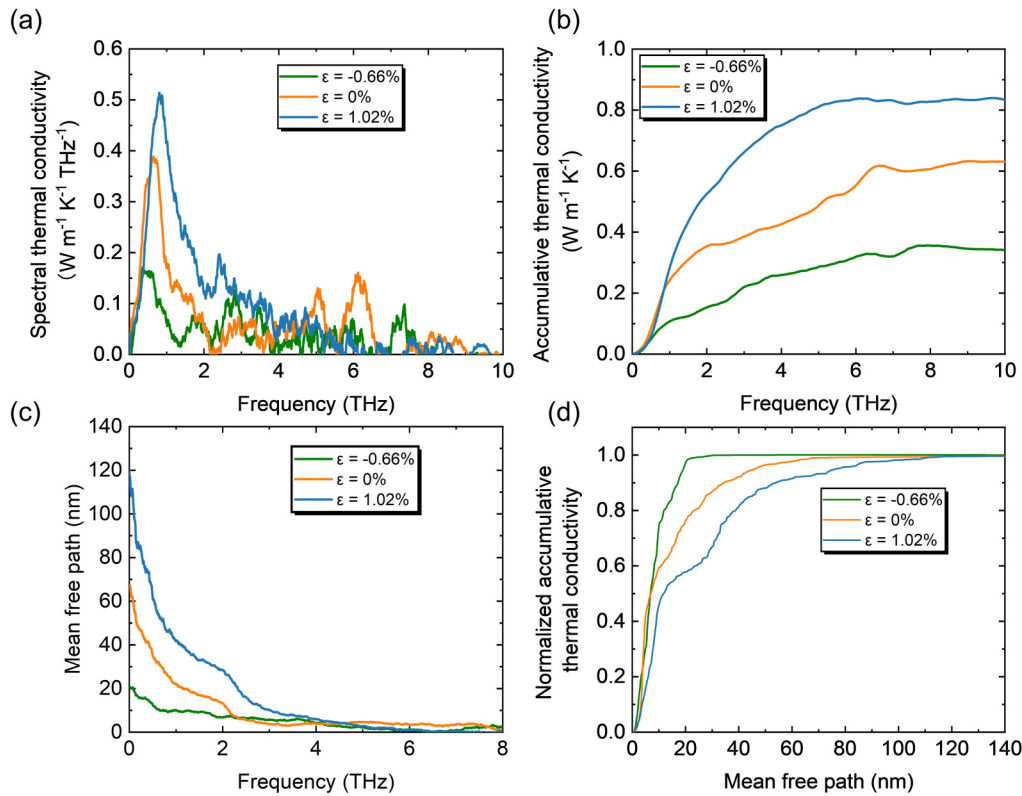


FIG. 3. (a) The spectral thermal conductivities of HKUST-1 under strains of -0.66 , 0 , and 1.02% . (b) The accumulative thermal conductivity of HKUST-1 under strains of -0.66 , 0 , and 1.02% . (c) The corresponding mean free path (MFP) of HKUST-1 under strains of -0.66 , 0 , and 1.02% . (d) The normalized accumulative thermal conductivities vs MFPs of HKUST-1 under strains of -0.66 , 0 , and 1.02% .

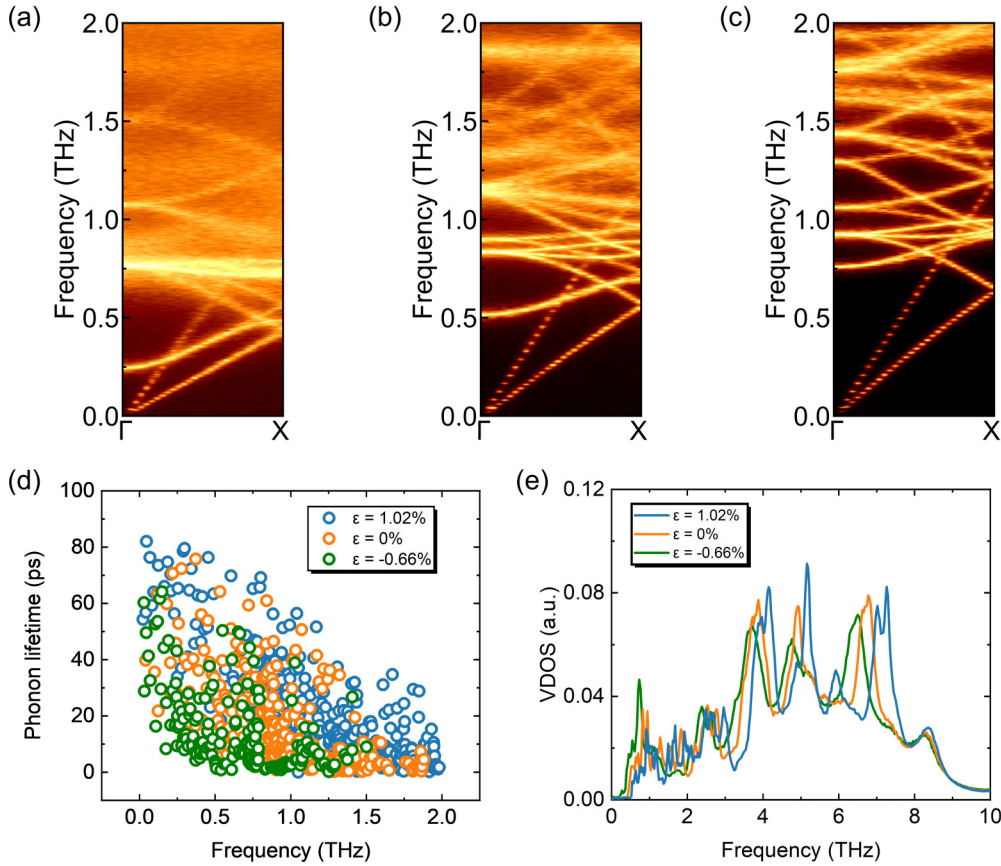


FIG. 4. The calculated spectral energy density (SED) of HKUST-1 under strains of (a) -0.66% , (b) 0% , and (c) 1.02% . (d) The phonon lifetimes calculated based on the SED results. (e) The vibrational density of states (VDOS) of HKUST-1 under different strains.

Authors of previous studies showed that the temperature dependence of the thermal conductivity for several MOFs, such as MOF-5 [11,12], ZIF-4, and ZIF-62 [13,14] was weak, which might result from the coexistence of propagating and nonpropagating vibrational modes in MOFs, as suggested by Huang *et al.* [11,12] and Zhou *et al.* [13,14]. For instance, Zhou *et al.* [13,14] quantified the vibrations in ZIF-4 and ZIF-62 based on the comparison between the vibrational MFPs and the minimal interatomic distance (MID) and found that many vibrations have MFPs shorter than the MID (i.e., nonpropagating vibrational modes). We emphasize that, while MOFs are crystals, the complex of the structures can introduce extremely strong anharmonicity and may lead to the emergence of nonpropagating vibrational modes. Here, we calculate the MFPs of vibrations in HKUST-1 considering external strain using Eq. (11) in Sec. II B. Our calculated results show that the MFPs of the original HKUST-1 without strain can be as long as 70 nm [Fig. 3(c)], and the MFPs of vibrations with frequency of 0–4 THz are generally larger than the MID of HKUST-1 (i.e., 0.5 nm, the distance between the metal atom and the center of organic sites). Thus, vibrations that contribute most to total thermal conductivity in HKUST-1 are propagating modes, which leads to a strong size effect of the corresponding thermal conductivity calculated using NEMD, as we have found before [23]. When tensile strain is applied to the system, the MFPs of these vibrations with frequencies <4 THz increase owing to the increased group

velocity and relaxation time (see the detailed analysis below). The MFPs of the vibrations with frequencies <2 THz in HKUST-1 decrease dramatically when compressive strain is applied. We further calculate the thermal conductivity function $\kappa(\Lambda_0) = \sum_{\Lambda < \Lambda_0} \kappa(\Lambda)$ and show the normalized $\kappa(\Lambda)$. The normalized accumulative thermal conductivity shows that the thermal conductivity in the compressed structure is mainly contributed by short MFP heat carriers [Fig. 3(d)]. This is because of the enhanced anharmonicity and reduced group velocity of these vibrations induced by the compressive strain (see the detailed analysis below). It is noted that our results will not change when HKUST-1 is depicted using NEP3 FF (Appendix A).

C. Vibrational scattering and group velocity considering strain

To further characterize the vibrational properties of HKUST-1 under different applied strains, we calculate the corresponding SED spectra using Eq. (12) in Sec. II B (Fig. 4). For pristine HKUST-1, the acoustic branches are more apparent [Fig. 4(b)]. The calculated vibrational relaxation times of pristine HKUST-1 range from ~ 20 to ~ 70 ps [Fig. 4(d)], and the corresponding average relaxation time of acoustic branches is ~ 40 ps. The scatterings among optical branches are strong due to the large out-of-phase movements among atoms enabled by the flexibility of the framework. For example, out-of-phase movements such as the trampolinelike

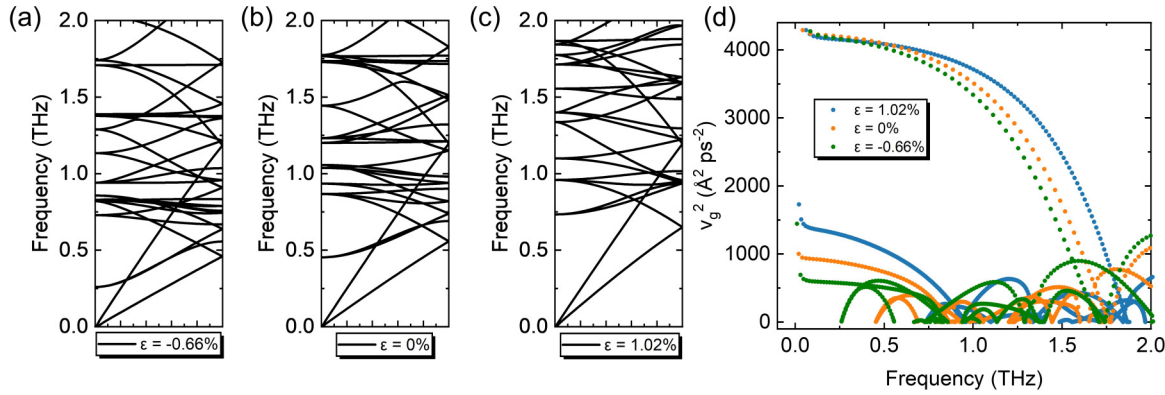


FIG. 5. The phonon dispersions of HKUST-1 under strains of (a) -0.66% , (b) 0% , and (c) 1.02% . (d) The square of the modal group velocity of HKUST-1 under different strains.

motion of organic linkers and the rotation of the Cu paddle wheel are found in HKUST-1 [50]. When HKUST-1 is under compression, the vibrational scatterings become much stronger [Fig. 4(a)], and the corresponding average relaxation time of vibrations is only ~ 21 ps [Fig. 4(d)]. This is because the applied compressive strain will increase the anharmonicity largely in HKUST-1 (see details in Sec. III D). On the contrary, the anharmonicity in HKUST-1 is found to become weaker when the tensile strain is applied, and the vibrational branches become much more apparent [Fig. 4(c)]. Consequently, the vibrational relaxation times of acoustic branches in stretched HKUST-1 (i.e., $\epsilon = 1.02\%$) range from ~ 30 to ~ 80 ps [Fig. 4(d)], and the average relaxation time of acoustic branches is ~ 59 ps. The SED spectra calculated using NEP3 FF show a similar trend to the results computed using Zhao's FF (Appendix A), which once again proves our calculated unusual pressure-dependent thermal conductivity of HKUST-1 is physical and reasonable.

Meanwhile, the vibrational branches are generally shifted downward (upward) owing to the structural softening (hardening) when external compressive (tensile) strain is applied [Figs. 4(a)–4(c) and Appendix A]. We further calculate the vibrational density of states (VDOS) and phonon dispersions of HKUST-1 and find that all the vibrations are shifted downward (upward) when external compressive (tensile) strain is applied [Figs. 4(e) and 5]. The downward (upward) shift of vibrational branches will not only increase (decrease) the possible scattering channels but also decrease (increase) the vibrational group velocity [Fig. 5(d)]. In addition, since Young's modulus can be estimated by the equation $E_Y = v^2 \rho$, in which E_Y is Young's modulus, ρ is density, and v is the speed of sound, the reduced group velocity of acoustic phonons near the center of the Brillouin zone demonstrates the softening and hardening of the structure when strain is applied. Based on the phonon-gas model, i.e., $\kappa \sim c_V v_g^2 \tau$, the decrease (increase) of group velocity may reduce (improve) the corresponding thermal conductivity. For instance, the mean longitudinal acoustic phonon relaxation time is reduced from ~ 370 to ~ 80 ps when a pressure of 19 GPa is applied to MoS₂, while the thermal conductivity of MoS₂ is increased by seven times due to the large improvement of group velocity [51]. As a result, the downward (upward) shift of vibrational branches caused by compressive (tensile) strain

can decrease (increase) the thermal conductivity, as we have shown in Fig. 1.

D. Anharmonicity in strained HKUST-1

As discussed above, the strain-dependent thermal conductivity of HKUST-1 stems from both the change of anharmonicity and the structural softening/hardening. In this section, we qualitatively quantify the change of anharmonicity in HKUST-1 induced by the applied external strain. We first trace the time-dependent atomic trajectories of HKUST-1 at 300 K under strains of -0.66 , 0 , and 1.02% and project them onto the $\{100\}$ lattice plane (Fig. 6). Therefore, Fig. 6 is a superposition of many frames at different times, and the trajectory represents the range that the atoms travel in space. It can be observed that atoms in all the structures under various strains vibrate around their equilibrium positions, following a feature of crystal structures. This may also be the reason that all vibrations in HKUST-1 under various strains are propagating modes. However, we can clearly observe that the vibrational amplitudes of atoms in HKUST-1 decrease when the applied strain changes from compressive to tensile (Fig. 6). It is shown that applied strain will strongly affect the atomistic vibrations in HKUST-1. We find that the interspace between adjacent atoms in HKUST-1 decreases or increases when compressive or tensile strain is applied, respectively. The interference of atomic vibrations in compressed (stretched) HKUST-1 becomes stronger (weaker) compared with that in pristine HKUST-1, which may affect the anharmonicity of vibrations in the systems. We further calculate the atomic mean square displacement (MSD), which is used to characterize the displacement of an atom from its equilibrium position. Our calculated MSDs show that the atomic displacement in compressed (stretched) structures is larger (smaller) than that in the pristine structure [Fig. 7(a)]. The larger atomic MSD indicates that atoms deviate farther from their equilibrium positions, which therefore causes larger anharmonic potential energy [Figs. 7(b)–7(d)]. As a result, the anharmonicity in HKUST-1 becomes stronger or weaker than that in pristine HKUST-1. More interestingly, we find that the MSD of the organic linker in HKUST-1 increases more apparently than that of the metal node. This is because organic linkers have small atomic mass and good flexibility.

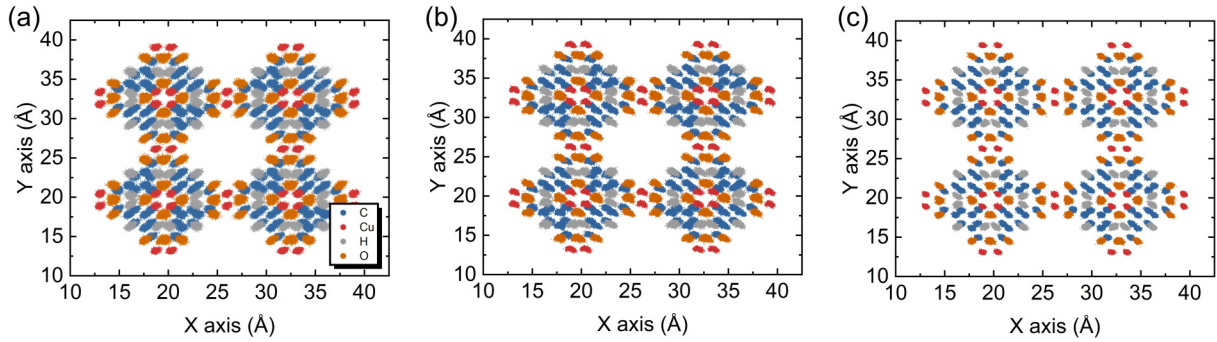


FIG. 6. The projected trajectories of atoms in HKUST-1 under strains of (a) -0.66% , (b) 0% , and (c) 1.02% .

The motions of the organic linker and metal node are significantly depressed in stretching. The influences of strain on the motions of framework atoms are also captured by NEP3 FF (Appendix B).

IV. CONCLUSIONS

In conclusion, the thermal transport in HKUST-1 considering mechanical strain is systematically investigated using MD simulations. Our calculated results show the thermal conductivity of HKUST-1 decreases (increases) with externally applied compressive (tensile) strain, which is contrary to the classical LS theory. This abnormal strain-dependent thermal conductivity of HKUST-1 is still observed when HKUST-1 is depicted using three different FFs. Our spectral

analysis shows that the anomalous strain-dependent thermal conductivity can be attributed to strain-induced variations in phonon properties, and the thermal transport in strained HKUST-1 can be depicted by the phonon-gas theory. The negative strain-dependent thermal conductivity (i.e., $\frac{dk}{dp} < 0$) under compression stems from the reduction of vibrational relaxation times and group velocities. We find that the anharmonicity in HKUST-1 becomes stronger when compression is applied, which leads to a large reduction of vibrational relaxation times. The compression-induced downward frequency shift of vibrational branches that results from the structural softening also decreases the vibrational group velocities largely. As a result, while the volumetric heat capacity increases, the thermal conductivity of HKUST-1 decreases with compression. When tensile strain is applied on HKUST-1,

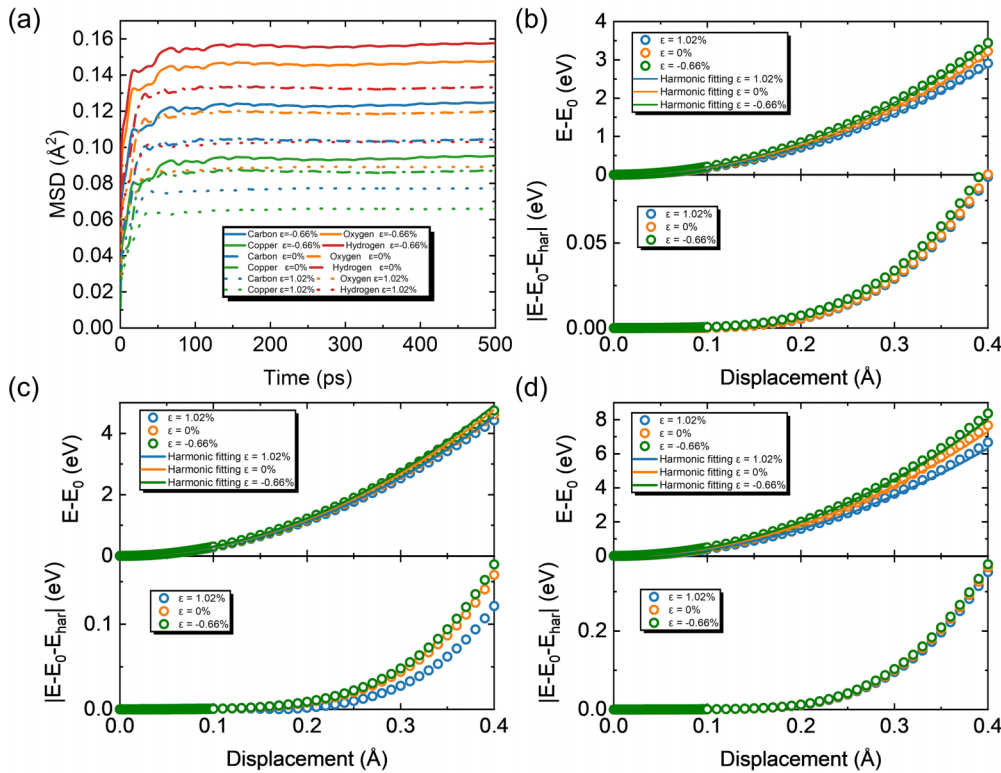


FIG. 7. (a) The mean square displacement of various atoms in HKUST-1 under strains of -0.66 , 0 , and 1.02% . The top panels are the potential energy changes (points) and corresponding harmonic fits (lines), and the bottom panels are the anharmonic energy of (b) oxygen atoms, (c) carbon atoms, and (d) copper atoms with displacements under different strains. The potential energy of hydrogen is not considered here.

the interspace between adjacent atoms increases, and the interference of atomic vibrations becomes weaker, which therefore decreases the anharmonicity and increases the vibrational relaxation times. Meanwhile, the vibrational group velocities are found to increase as the vibrational branches shift upward owing to the structural hardening. Therefore, the thermal conductivity of HKUST-1 increases with external tensile strain. Our findings here uncover the mechanism of the abnormal strain-dependent thermal conductivity of HKUST-1, which may guide the design of future thermal-related applications of MOFs.

ACKNOWLEDGMENTS

Y.Z. acknowledges the Startup Fund (Grant No. REC20EGR14, a/c-R9246) and Frontier Technology Research for Joint Institutes with Industry Scheme (Grant No. FTRIS-002) from the Hong Kong University of Science and Technology. Z.L., Y.C., and Y.Z. acknowledge the fund from Research Grants Council of the Hong Kong Special Administrative Region under Grant No. C6020-22G. Y.Z. also thanks the Hong Kong SciTech Pioneers Award from the Y-LOT foundation. This paper was supported in part by the Project of Hetao Shenzhen-Hong Kong Science and Technology Innovation Cooperation Zone (No. HZQB-KCZYB-2020083).

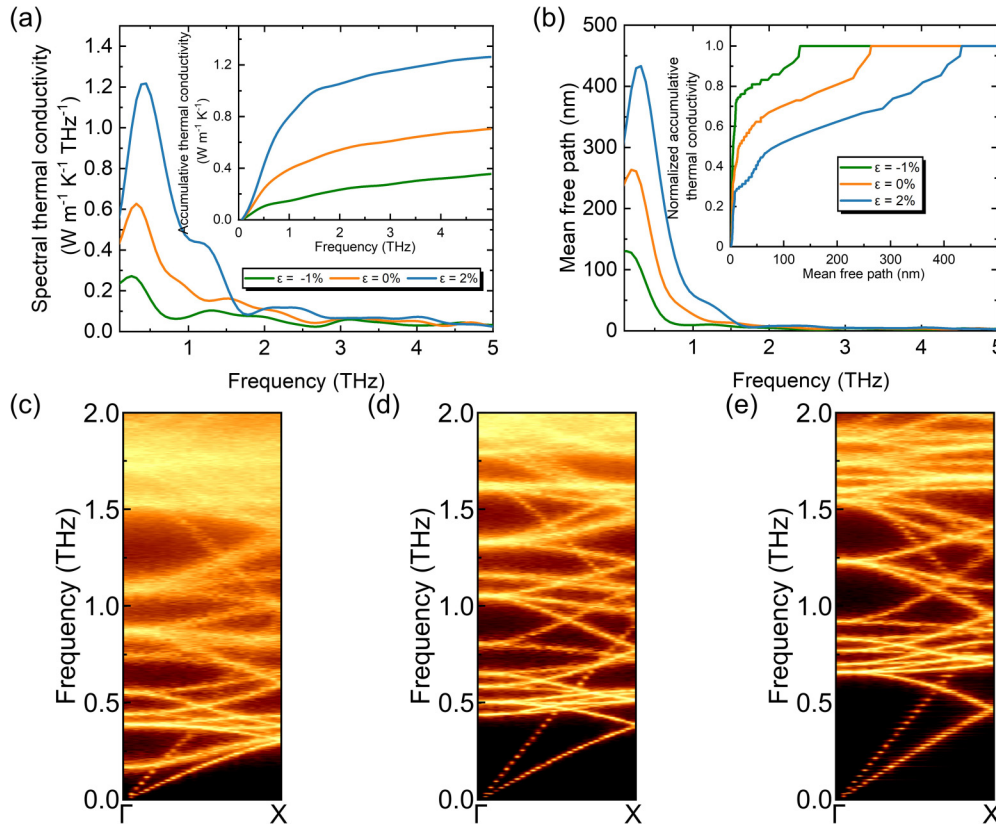


FIG. 8. (a) The spectral thermal conductivity of HKUST-1 depicted by the third generation of neuroevolution potential (NEP3) force field (FF) under strains of -1% , 0% , and 2% , in which the inset is the accumulative thermal conductivity. (b) The corresponding mean free path (MFP) of HKUST-1 depicted by NEP3 FF under strains of -1% , 0% , and 2% , in which the inset is the normalized accumulative thermal conductivity vs MFPs (MFPs) under strains of -1% , 0% , and 2% . The SED of HKUST-1 depicted by NEP3 FF under strains of (c) -1% , (d) 0% , and (e) 2% .

APPENDIX A: SPECTRAL VIBRATION PROPERTIES EVALUATED BY NEP3 FF

In our paper, three different FFs were adopted to describe the interatomic interactions of HKUST-1. These three FFs give a consistent strain-dependent thermal conductivity of HKUST-1. Both Zhao's and Wieme's FFs are constructed using analytic functions. Only the calculations based on Zhao's FF are used to carry out our analysis. The calculations based on NEP3 FF are implemented using GPUMD, which is different from the calculations based on Zhao's and Wieme's FFs. We therefore need to evaluate the spectral vibrational properties of HKUST-1 in the GPUMD simulations where the interatomic interactions are depicted using NEP3 FF. The spectral thermal conductivity calculated based on NEP3 FF also shows that the contribution of low-frequency vibrations is largely reduced with strains changing from tensile to compressive [Fig. 8(a)]. The corresponding MPFs are decreased (increased) when compressive (tensile) strain is applied [Fig. 8(b)]. While the spectral thermal conductivity and MPFs calculated based on NEP3 FF are slightly different, the results based on NEP3 and Zhao's FFs reveal the same influences of mechanical strain on the spectral vibrational properties of HKUST-1. Our SED calculations based on NEP3 FF also show that the phonon scatterings become stronger (weaker), and the vibrational frequency is shifted down (up) when compressive (tensile) strain is applied [Figs. 8(c)–8(e)]. Meanwhile, the scatterings among

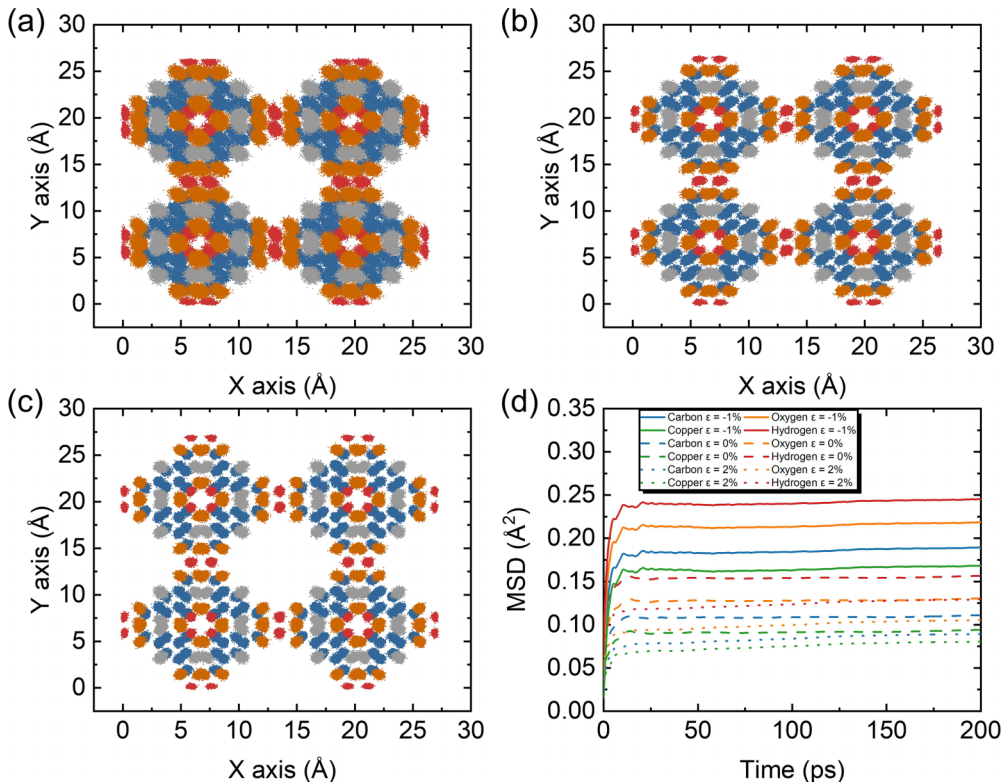


FIG. 9. The projected trajectories of atoms in HKUST-1 depicted by the third generation of neuroevolution potential (NEP3) force field (FF) under strains of (a) -1% , (b) 0% , and (c) 2% . (d) The mean square displacement of various atoms in HKUST-1 depicted by NEP3 FF under strains of -1 , 0 , and 2% .

phonons are largely increased when HKUST-1 is compressed, which indicates a reduction of vibrational group velocity and lifetime [Fig. 8(c)].

APPENDIX B: INFLUENCES OF STRAIN ON ATOMIC MOTIONS EVALUATED BY NEP3 FF

In our above discussions, the anharmonicity of HKUST-1 is quantified by the atomistic trajectories and their

deviations from the corresponding equilibrium positions. Here, the atomic trajectories of HKUST-1 depicted by NEP3 FF also show that all atoms vibrate around their equilibrium positions, and interatomic distance is disparate in HKUST-1 under various mechanical strains [Figs. 9(a)–9(c)]. The MSD of different atoms calculated based on NEP3 FF also shows that their vibrational amplitudes in the compressed HKUST-1 are larger than that in the stretched HKUST-1, indicating a stronger anharmonicity in the compressed HKUST-1.

-
- [1] S. Salehi and M. Anbia, High CO_2 adsorption capacity and CO_2/CH_4 selectivity by nanocomposites of MOF-199, *Energy Fuels* **31**, 5376 (2017).
 - [2] J. Wieme, S. Vandenbrande, A. Lamine, V. Kapil, L. Vanduyfhuys, and V. Van Speybroeck, Thermal engineering of metal-organic frameworks for adsorption applications: A molecular simulation perspective, *ACS Appl. Mater. Interfaces* **11**, 38697 (2019).
 - [3] K. J. Chang and O. Talu, Behavior and performance of adsorptive natural gas storage cylinders during discharge, *Appl. Therm. Eng.* **16**, 359 (1996).
 - [4] S. Ma and H.-C. Zhou, Gas storage in porous metal-organic frameworks for clean energy applications, *Chem. Commun.* **46**, 44 (2010).
 - [5] H. Wang, Z. Qu, Y. Yin, J. Zhang, and P. Ming, Thermal management for hydrogen charging and discharging in a screened metal-organic framework particle tank, *ACS Appl. Mater. Interfaces* **13**, 61838 (2021).
 - [6] L. Han, M. Budge, and P. Alex Greaney, Relationship between thermal conductivity and framework architecture in MOF-5, *Comput. Mater. Sci.* **94**, 292 (2014).
 - [7] S. Zhang, J. Liu, and L. Liu, Insights into the thermal conductivity of MOF-5 from first principles, *RSC Adv.* **11**, 36928 (2021).
 - [8] P. Ying, J. Zhang, X. Zhang, and Z. Zhong, Impacts of functional group substitution and pressure on the thermal conductivity of ZIF-8, *J. Phys. Chem. C* **124**, 6274 (2020).
 - [9] L. Lindsay, D. A. Broido, J. Carrete, N. Mingo, and T. L. Reinecke, Anomalous pressure dependence of thermal conductivities of large mass ratio compounds, *Phys. Rev. B* **91**, 121202(R) (2015).
 - [10] H. Ehrenreich, F. Seitz, and D. Turnbull, *Solid State Physics*, 1st ed. (Academic Press, New York, 1979), Vol. 34.

- [11] B. L. Huang, Z. Ni, A. Millward, A. J. H. McGaughey, C. Uher, M. Kaviani, and O. Yaghi, Thermal conductivity of a metal-organic framework (MOF-5): Part II, Measurement, *Int. J. Heat Mass Transf.* **50**, 405 (2007).
- [12] B. L. Huang, A. J. H. McGaughey, and M. Kaviani, Thermal conductivity of metal-organic framework 5 (MOF-5): Part I. Molecular dynamics simulations, *Int. J. Heat Mass Transf.* **50**, 393 (2007).
- [13] Y. Zhou, Y. Xu, Y. Gao, and S. Volz, Origin of the weakly temperature-dependent thermal conductivity in ZIF-4 and ZIF-62, *Phys. Rev. Mater.* **6**, 015403 (2022).
- [14] Y. Zhou, B. Huang, and B.-Y. Cao, Vibrational modes with long mean free path and large volumetric heat capacity drive higher thermal conductivity in amorphous zeolitic imidazolate framework-4, *Mater. Today Phys.* **21**, 100516 (2021).
- [15] L. Zhao, Q. Yang, Q. Ma, C. Zhong, J. Mi, and D. Liu, A force field for dynamic Cu-BTC metal-organic framework, *J. Mol. Model.* **17**, 227 (2011).
- [16] Z. Fan, Y. Wang, P. Ying, K. Song, J. Wang, Y. Wang, Z. Zeng, K. Xu, E. Lindgren, J. Magnus Rahm *et al.*, GPUMD: A package for constructing accurate machine-learned potentials and performing highly efficient atomistic simulations, *J. Chem. Phys.* **157**, 114801 (2022).
- [17] Q. Yang and C. Zhong, Molecular simulation of carbon dioxide/methane/hydrogen mixture adsorption in metal+-organic frameworks, *J. Phys. Chem. B* **110**, 17776 (2006).
- [18] S. L. Mayo, B. D. Olafson, and W. A. Goddard, DREIDING: A generic force field for molecular simulations, *J. Phys. Chem.* **94**, 8897 (1990).
- [19] A. K. Rappe, C. J. Casewit, K. S. Colwell, W. A. I. Goddard, and W. M. Skiff, UFF, a full periodic table force field for molecular mechanics and molecular dynamics simulations, *J. Am. Chem. Soc.* **114**, 10024 (1992).
- [20] M. Islamov, H. Babaei, and C. E. Wilmer, Influence of missing linker defects on the thermal conductivity of metal-organic framework HKUST-1, *ACS Appl. Mater. Interfaces* **12**, 56172 (2020).
- [21] K. J. Erickson, F. Léonard, V. Stavila, M. E. Foster, C. D. Spataru, R. E. Jones, B. M. Foley, P. E. Hopkins, M. D. Allendorf, and A. A. Talin, Thin film thermoelectric metal-organic framework with high Seebeck coefficient and low thermal conductivity, *Adv. Mater.* **27**, 3453 (2015).
- [22] M. Agrawal, S. E. Boulfelfel, D. F. Sava Gallis, J. A. Greathouse, and D. S. Sholl, Determining diffusion coefficients of chemical warfare agents in metal-organic frameworks, *J. Phys. Chem. Lett.* **10**, 7823 (2019).
- [23] H. Fan, C. Yang, and Y. Zhou, Ultralong mean free path phonons in HKUST-1 and their scattering by water adsorbates, *Phys. Rev. B* **106**, 085417 (2022).
- [24] Z. Fan, Improving the accuracy of the neuroevolution machine learning potential for multi-component systems, *J. Phys.: Condens. Matter* **34**, 125902 (2022).
- [25] S. Plimpton, Fast parallel algorithms for short-range molecular dynamics, *J. Comput. Phys.* **117**, 1 (1995).
- [26] R. W. Hockney and J. W. Eastwood, *Computer Simulation Using Particles* (Taylor & Francis, New York, 1988).
- [27] D. J. Evans and B. L. Holian, The Nosé-Hoover thermostat, *J. Chem. Phys.* **83**, 4069 (1985).
- [28] deepmodeling/dpdata, <https://github.com/deepmodeling/dpdata>.
- [29] J. P. Perdew, K. Burke, and M. Ernzerhof, Generalized gradient approximation made simple, *Phys. Rev. Lett.* **77**, 3865 (1996).
- [30] P. E. Blöchl, Projector augmented-wave method, *Phys. Rev. B* **50**, 17953 (1994).
- [31] G. Kresse and J. Furthmüller, Efficient iterative schemes for *ab initio* total-energy calculations using a plane-wave basis set, *Phys. Rev. B* **54**, 11169 (1996).
- [32] G. Kresse and D. Joubert, From ultrasoft pseudopotentials to the projector augmented-wave method, *Phys. Rev. B* **59**, 1758 (1999).
- [33] P. Ying, T. Liang, K. Xu, J. Zhang, J. Xu, Z. Zhong, and Z. Fan, Sub-micrometer phonon mean free paths in metal-organic frameworks revealed by machine learning molecular dynamics simulations, *ACS Appl. Mater. Interfaces* **15**, 36412 (2023).
- [34] Z. Fan, H. Dong, A. Harju, and T. Ala-Nissila, Homogeneous nonequilibrium molecular dynamics method for heat transport and spectral decomposition with many-body potentials, *Phys. Rev. B* **99**, 064308 (2019).
- [35] Y. Zhou and M. Hu, Quantitatively analyzing phonon spectral contribution of thermal conductivity based on nonequilibrium molecular dynamics simulations. II. From time Fourier transform, *Phys. Rev. B* **92**, 195205 (2015).
- [36] Y. Zhou and M. Hu, Full quantification of frequency-dependent interfacial thermal conductance contributed by two- and three-phonon scattering processes from nonequilibrium molecular dynamics simulations, *Phys. Rev. B* **95**, 115313 (2017).
- [37] K. Sääskilahti, J. Oksanen, J. Tulkki, and S. Volz, Role of anharmonic phonon scattering in the spectrally decomposed thermal conductance at planar interfaces, *Phys. Rev. B* **90**, 134312 (2014).
- [38] K. Sääskilahti, J. Oksanen, S. Volz, and J. Tulkki, Frequency-dependent phonon mean free path in carbon nanotubes from nonequilibrium molecular dynamics, *Phys. Rev. B* **91**, 115426 (2015).
- [39] J. Wang and J.-S. Wang, Carbon nanotube thermal transport: Ballistic to diffusive, *Appl. Phys. Lett.* **88**, 111909 (2006).
- [40] T. Yamamoto, S. Konabe, J. Shiomi, and S. Maruyama, Crossover from ballistic to diffusive thermal transport in carbon nanotubes, *Appl. Phys. Express* **2**, 095003 (2009).
- [41] L. G. C. Rego and G. Kirczenow, Quantized thermal conductance of dielectric quantum wires, *Phys. Rev. Lett.* **81**, 232 (1998).
- [42] S. Datta, *Electronic Transport in Mesoscopic Systems* (Cambridge University Press, Cambridge, 1997).
- [43] J. A. Thomas, J. E. Turney, R. M. Iutzi, C. H. Amon, and A. J. H. McGaughey, Predicting phonon dispersion relations and lifetimes from the spectral energy density, *Phys. Rev. B* **81**, 081411(R) (2010).
- [44] A. J. C. Ladd, B. Moran, and W. G. Hoover, Lattice thermal conductivity: A comparison of molecular dynamics and anharmonic lattice dynamics, *Phys. Rev. B* **34**, 5058 (1986).
- [45] J. Farrando-Pérez, M. Rodríguez-Castillo, M. Martínez-Escandell, M. Monge, and J. Silvestre-Albero, Improved thermal management in HKUST-1 composites upon graphite flakes incorporation: Hydrogen adsorption properties, *Int. J. Hydrogen Energy* **48**, 36474 (2023).
- [46] N. Moitra, S. Fukumoto, J. Reboul, K. Sumida, Y. Zhu, K. Nakanishi, S. Furukawa, S. Kitagawa, and K. Kanamori, Mechanically stable, hierarchically porous Cu₃(btc)₂ (HKUST-1)

- monoliths via direct conversion of copper(II) hydroxide-based monoliths, *Chem. Commun.* **51**, 3511 (2015).
- [47] Z. Zeng, Y. Xiao, J. M. Wheeler, and J.-C. Tan, *In situ* micropillar compression of an anisotropic metal-organic framework single crystal, *Commun Chem* **6**, 63 (2023).
- [48] G. Leibfried and E. Schrömann, Wärmeleitung in elektrisch isolierenden Kristallen, *Nach. Akad. Wiss. Göttingen Math. Phys. Klasse* **4**, 71 (1954).
- [49] S. S. Sørensen, M. B. Østergaard, M. Stepniewska, H. Johra, Y. Yue, and M. M. Smedskjaer, Metal-organic framework glasses possess higher thermal conductivity than their crystalline counterparts, *ACS Appl. Mater. Interfaces* **12**, 18893 (2020).
- [50] M. R. Ryder, B. Civalleri, G. Cinque, and J.-C. Tan, Discovering connections between terahertz vibrations and elasticity underpinning the collective dynamics of the HKUST-1 metal-organic framework, *CrystEngComm* **18**, 4303 (2016).
- [51] X. Meng, T. Pandey, J. Jeong, S. Fu, J. Yang, K. Chen, A. Singh, F. He, X. Xu, J. Zhou *et al.*, Thermal conductivity enhancement in MoS₂ under extreme strain, *Phys. Rev. Lett.* **122**, 155901 (2019).